Modeling the flow around and the hydrodynamic drag on net meshes using REEF3D

Gang Wang [1, 2, *], Tobias Martin [2], Liuyi Huang [1], Hans Bihs [2]

1 College of Fisheries, Ocean University of China, Qingdao 266003, China

2 Department of Civil and Environmental Engineering, Norwegian University of Science and Technology, Trondheim 7491, Norway

Gang Wang[*], (corresponding author)wg@stu.ouc.edu.cn

Abstract

The hydrodynamics and flow around net meshes has recently drawn more and more attention because it is closely related to the expected forces on aquaculture. In terms of modelling the hydrodynamic forces on nets, Morison or screen force models are ordinarily. However, they mainly rely on empirical, experimental or cylindrical hydrodynamic coefficients, neglecting the flow interactions between adjacent net twines. In this study, the open-source hydrodynamic toolbox REEF3D is adopted to analyze the flow around net meshes and investigate the hydrodynamic drag on the structure. The simulation accuracy is in good agreement with flume experiments and previous research. The results demonstrate that 2×2 or 3×3 mesh cases are more reliable for studying the flow around net meshes including the flow interactions around adjacent twines. It is further shown that controlling the solidity of the net through changing net bar diameters has different effects on the flow around meshes than controlling it by the twine length. This paper presents a first step in the aim to derive a new empirical formula for the drag coefficients depending on the solidity and fluid properties which is more appropriate for to the physics involved in offshore conditions.

Keywords: Fishing nets; Hydrodynamics; CFD; Drag forces

1 Introduction

Due to the pollution and the increase of aquaculture in coastal areas, the fish farming industry tends to move to the offshore area. Open ocean aquaculture facilities are typically more complicated and increased in size compared to traditional flexible floating cage. Meanwhile, since the sea environment loadings in deep water are more severe than in near-shore areas, fish farms experience large dynamic responses and deformations of the nets leading to fatigues or unpredictable damages [1]. The nets of fish farms in extreme wave-current loadings risk collision with fish which leads to the damage of the net meshes [2]. The hydrodynamics around the net meshes used in offshore fish farms are still not investigated with respect to flow interaction effects. Therefore, it is crucial to study the flow around net meshes adopted in offshore fish farms.

The diameters and lengths of net meshes are small while other components of fish farms are of the size of incident waves. This implies significant difficulties in carrying out flume experiments if the details of the flow around the net meshes and inside cages are of interest. Besides, flow conditions inside the fish cage using Computational Fluid Dynamics (CFD) and fluid-structure interaction (FSI) of nets are still ongoing research [3]. It is promising to study the flow around and hydrodynamics loadings on net meshes using CFD in order to gain knowledge about the flow around meshes. Numerous researchers have analysed the hydrodynamics loadings on net panels and proposed different semi-empirical formulas based on experiments, but no standard coefficients are derived holding various structural factors. The normal and tangential drag coefficient (C_d) of each mesh line based on the Reynolds number (Re) was studied in [4], but other structural factors or interactions among net twines were not included. In [5], a relation between the normal C_d and the solidity ratio (S_n) applied to square net meshes of knotless and nets with knots were derived using experiments. As presented in [6], C_d and the lift coefficient of net panels related to S_n and the Angle of Attack (AOA) were analysed based on experiments, especially the irrelevance between C_d and AOA when the panel was parallel to the incoming flow, that is, AOA=0°, was emphasized. Considering the hydrodynamics, it seems insufficient to use S_n as the exclusive parameter, and this is can be shown by studying the parameters related to the flow properties around meshes. In [7], normal and tangential C_d were deduced as the function of velocity and S_n through Nylon plane nets measurements with diamond meshes. The analytical C_d of the circular cylinder proposed by [8] was promoted for nets in [9], taking Re and S_n into consideration simultaneously. As shown in [10], the hydrodynamics of Nylon fishing nets were physically measured. The results for Re ranging from 430

to 5742 and AOA ranging from 10° to 90° showed dependencies of C_d on these two factors. However, lift coefficients were only dependent on AOA since they overlooked the minor *Re* effect. The screen net force model, implying the hydrodynamics loadings on the decomposed screen sheet, was developed in [11]. In [12], flume experiments were conducted to analyze the hydrodynamics loadings on an isolated cruciform depicting a single net mesh. Further, a semi-empirical formula was derived experimentally by studying the hydrodynamics of plane nets, combining S_n with AOA and *Re* [13~14]. However, because the research mainly studied meshes of purse seine with small S_n, hydrodynamics of nets with a wide range of S_n were not discussed. For FSI research, the flow effects over nets were modelled numerically using porous media [15~18, 36]. Here, wake zones behind nets and the velocity reduction were simulated, but details regarding flow around the net meshes lacked as the porous media strategy was used. Afterward, a high-resolution CFD simulation of the flow around net meshes was investigated in [19], velocity profiles around net meshes were extracted across several critical locations, and the AOA and mesh orientation influences on flow patterns were explicitly analysed.

It is therefore of interest to carry out numerical simulations of the flow around and hydrodynamics loadings on net meshes in order to improve existing numerical models for fluid-net interaction. Here, 1×1, 2×2, and 3×3 meshes are considered. Then, comparisons of the flow fields around various dimensions of net panel portions are presented, aiming to discuss the appropriate number of meshes in a numerical study. Compared to the earlier work studying net meshes using CFD techniques [19], the flow interactions resulting from multiple net meshes are illustrated. The implications among flow properties, hydrodynamic drag on net meshes, and solidity factor are introduced through CFD methods for the first time, revealing the distributions of time-averaged pressure and instantaneous vorticity patterns. The correlations between hydrodynamic loadings and flow properties are described as well. S_n and *Re* are utilized as the main factors defining the net meshes. The structural response of the net is ignored due to the very small geometrical scale. The simulations are performed using the open-source hydrodynamics code REEF3D [20], which has been validated for numerous applications in offshore engineering fields, such as breaking wave forces [21, 33~35] and fluid-structure interaction of floating structures and nets [22, 36~37].

The structure of this paper is presented as follows: details about the chosen geometry for the net meshes, numerical methods and the relevant validations predicting hydrodynamic loadings and flow fields, are presented in Section 2. Then, the results of simulations are discussed with respect to flow fields

and hydrodynamic drags on the net meshes with varying S_n and Re in Section 3, where in a semi-empirical formula is proposed based on the numerical simulations. Finally, the highlights and conclusions are summarized in Section 4.

2 Material and methods

2.1 Net meshes

The net mesh model in this study is the prototype used in the inner nets of Deep Blue I, the largest offshore fish farm in China (Fig. 1). In general, inner nets are exposed to several kinds of loading, including hydrodynamic loadings and the related interactions with fish. The prototype has the square twisted knotless meshes with a constant solidity ratio of 0.28, of which the diameter and length of each mesh twine is 3 mm and 2 cm, respectively (Fig. 1). The nets material is Ultra High Molecular Weight Polyethylene Fiber (UHMWPE), which is widely used in the aviation and ocean industry.

Fig. 1: Deep Blue I and its prototype mesh

2.2 Numerical modelling

The incompressible fluid flow is described by the three-dimensional Unsteady Reynolds-Averaged Navier-Stokes equations (URANS), which are solved together with the continuity equation for describing the momentum and mass conservation (Eqn. 1).

$$\frac{\partial u_i}{\partial x_i} = 0 \tag{1}$$

$$\frac{\partial u_i}{\partial t} + u_j \frac{\partial u_i}{\partial x_j} = -\frac{1}{\rho}\frac{\partial p}{\partial x_i} + \frac{\partial}{\partial x_j}\left[(\nu + \nu_t)\left(\frac{\partial u_i}{\partial x_j} + \frac{\partial u_j}{\partial x_i}\right)\right] + g_i$$

where u is the velocity averaged over time t, ρ is the fluid density, p is the pressure, ν is the kinematic viscosity, ν_t is the eddy viscosity and g the acceleration due to gravity. The eddy viscosity ν_t in the URANS equations is modelled using the two-equation k-ω model [23].

The convective and diffusion terms of the URANS equations are discretized with the five-order

WENO scheme [20] in the conservative finite-difference framework. For the time treatment of the momentum equations, a third-order accurate TVD Runge–Kutta scheme was employed. Diffusion terms of URANS equations are treated implicitly to ensure the stability of the calculations. These discretization schemes ensure numerical stability. Also, an adaptive time stepping strategy is used in REEF3D. Here, a constant CFL number, considering the effects from grid size, external velocity, and diffusion terms, is ensured throughout the simulation [20].

2.3 Boundary condition

A 3D Cartesian right-handed coordinate system is established in the numerical simulation, in which x is positive along the flow direction, z is perpendicular to the flow direction on the horizontal plane and y is perpendicular to the plane formed by x and z. The non-dimensional computational domain is approximately 214d in length, 143d in width and 143d in height, which is the same as in [19]. Here, d is the diameter of the cylinder. At the inlet, a uniform velocity is imposed, and zero gradient pressure outflow condition is used at the outlet. The surrounding boundaries in the domain are treated with symmetry conditions, which means the normal components of the velocity are set to zero and the normal gradients of all variables are zero. For initializing the k-ω model, the turbulent intensity I is given at the inlet boundary based on Eqn. 2. The surfaces of the net twines are implicitly defined as non-slip wall boundaries, and the near-surface velocity was modelled based on wall functions.

$$D_H = \frac{4A_c}{S_c}; Re_{D_H} = \frac{U_0 D_H}{\nu}; I = 0.16(Re_{D_H})^{-1/8} \tag{2}$$

where A_c and S_c are cross sectional area of computational domain in the x direction and perimeter of this cross section, respectively. U_0 denotes the undisturbed incoming velocity, D_H is the hydraulic diameter of flume tank and Re represents Reynolds number characterized by the hydraulic diameter.

2.4 Computational grids: Immersed Boundary method

In REEF3D, a ghost cell immersed boundary method (GCIBM) is used [20]. The method has been validated against previous studies and experiments [29~37]. The advantage of using the GCIBM lies in avoiding complicated procedures to generate high-quality around complex structures such as cruciform and high numerical stability. Additionally, the numerical discretization does not need to account for the boundary conditions explicitly. Instead, they are enforced implicitly. In this study, the uniform-sized

mesh (Fig. 2) based on GCIBM was adopted in the whole domain, and the cell number varies between 3.0×10^7 and 2.0×10^8. A uniform-sized mesh strategy is considered to ensure the accuracy of the flow field in the wake and the far-field area. REEF3D is fully parallelized using the domain decomposition method and MPI (Message passing interface) [20]. All the presented simulations are performed on Uninett Sigma2's supercomputer Fram on 256 processors. A typical simulation required 48~96 hours to be completed.

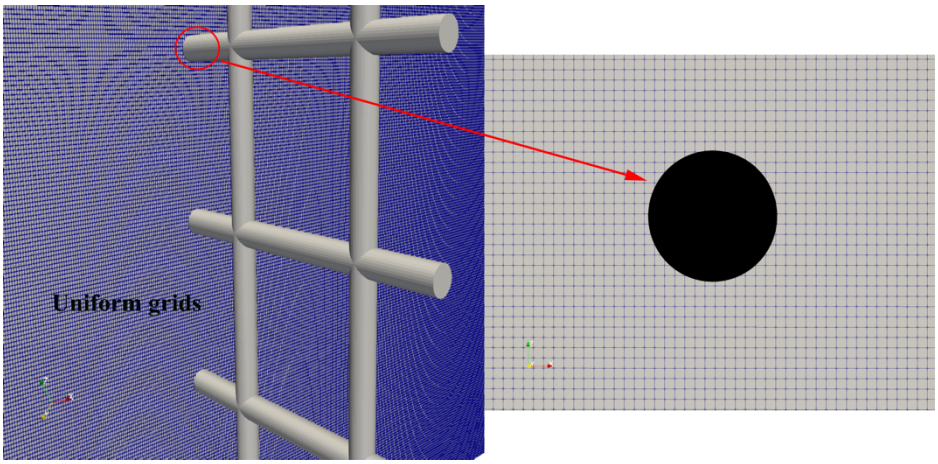

Fig. 2: Uniform-size computational grids around the net meshes

2.5 Data statistics and cases set-up

To study the hydrodynamics and flow around net meshes, the mean drag coefficient C_d is calculated using Eqn. 3.

$$C_d = \frac{F_d}{0.5\rho S U_0^2} \tag{3}$$

where F_d represents the time-averaged drag force and S is the projection area of the meshes.

The solidity ratio, S_n, describes the ratio of the projected area of the net over the total area, enclosed by the net. For the square mesh in this study, S_n is defined as follows (Eqn. 4) [34].

$$S_n = \frac{2*d}{l} - \left(\frac{d}{l}\right)^2 \tag{4}$$

where l and d denote lengths and diameters of each wire, respectively.

As the important geometrical factors, S_n and Re have the largest impacts on the hydrodynamics and flow around the net meshes. They are closely related to the incoming velocity as well as the diameter and length of the net bars. Two methods of changing S_n, using the diameter and length of each bar, are adopted in this study. All cases are shown in Tab. 1.

Tab. 1: Setup for the numerical cases.

Case	Dimension	d [mm]	l [cm]	Re	S_n
1	1*1	3.00	2.00	756.30	0.28
2	2*2	3.00	2.00	756.30	0.28
3	3*3	3.00	2.00	756.30	0.28
4	2*2	2.11	2.00	533.08	0.2
5	2*2	3.27	2.00	823.56	0.3
6	2*2	4.51	2.00	1136.49	0.4
7	2*2	5.86	2.00	1476.77	0.5
8	2*2	7.35	2.00	1853.17	0.6
9	2*2	3.00	2.84	756.30	0.2
11	2*2	3.00	1.33	756.30	0.4
12	2*2	3.00	1.02	756.30	0.5
13	2*2	3.00	0.82	756.30	0.6
14	2*2	3.00	2.84	1260.50	0.2
15	2*2	3.00	2.84	1764.71	0.2
16	2*2	3.00	2.84	2268.91	0.2
17	2*2	3.00	1.84	1260.50	0.3
18	2*2	3.00	1.84	1764.71	0.3
19	2*2	3.00	1.84	2268.91	0.3
20	2*2	3.00	1.33	1260.50	0.4
21	2*2	3.00	1.33	1764.71	0.4
22	2*2	3.00	1.33	2268.91	0.4
23	2*2	3.00	1.02	1260.50	0.5
24	2*2	3.00	1.02	1764.71	0.5
25	2*2	3.00	1.02	2268.91	0.5
26	2*2	3.00	0.82	1260.50	0.6
27	2*2	3.00	0.82	1764.71	0.6
28	2*2	3.00	0.82	2268.91	0.6
29	2*2	3.00	2.00	1260.50	0.28
30	2*2	3.00	2.00	1764.71	0.28
31	2*2	3.00	2.00	2268.91	0.28

2.6 Validations

To ensure that the flow through the net meshes and the hydrodynamics are captured sufficiently, the grid size around the structures has to be sufficiently small. Therefore, a mesh independence test is carried out for the time-averaged drag coefficient (C_d, Eqn. 3). A constant Reynolds number (Re) of 10^5 is used. The computational domain and the boundary conditions are kept the same as given in [24] to ensure comparability of various methods. The results can be found in Table 2. It is evident that the case with 40 cells (approximately 3.1×10^{-4} m) in the circumference of the cylinder is sufficient to analyze the hydrodynamic loadings on the cylindrical structure. In comparison, it would need 60 cells using a conforming mesh strategy and FVM [19]. For the validation of the flow field, the typical benchmark case of the flow around a circular cylinder at Re = 3900 is carried out against physical measurements and published large eddy simulations (LES) and direct numerical simulations (DNS). It is shown in Fig. 3 that the results using REEF3D follow the envelope of the mean streamwise velocity variations across the

side directions. The deviations are consistently below 10% compared to published data. Besides, the required time-step is verified through a convergence study for different CFL numbers. As illustrated in Fig. 3, only minor differences are observed across the cases for CFL numbers between 0.2 and 0.4. This is in accordance with the clarifications in [20] that the numerical stability is secured in this procedure. Therefore, a constant CFL number of 0.3 is utilized in the following investigations.

Tab. 2: Mesh independence test

Cells in circumference		Cell number		C_d	
16	&	6.2×10^4	&	1.286	\\
24	&	1.4×10^5	&	1.245	\\
32	&	2.5×10^5	&	1.266	\\
40	&	3.9×10^5	&	1.138	\\
48	&	5.6×10^5	&	1.081	\\
56	&	7.6×10^5	&	1.094	\\
64	&	1.0×10^6	&	1.104	\\

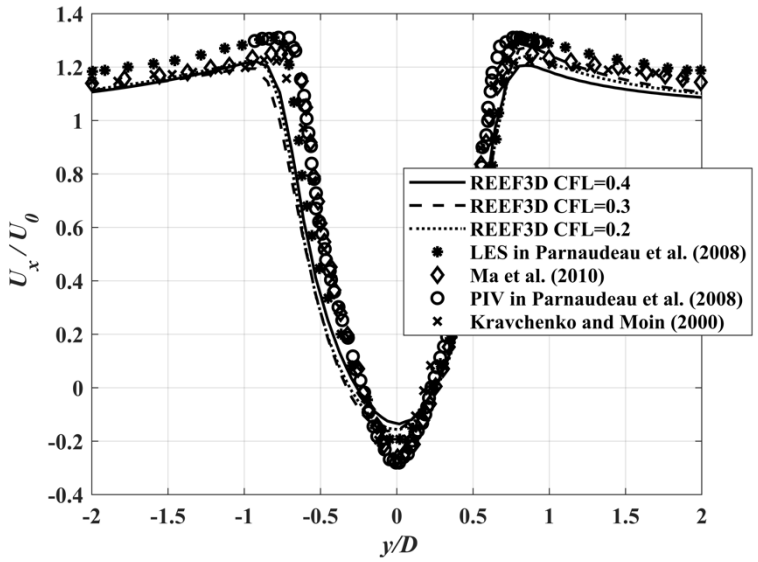

Fig. 3: The non-dimensional mean streamwise velocity across the side directions of cylinder at x / D = 1.54 when Re = 3900.

Vorticity $\boldsymbol{\omega}$, defined as the flow velocity curl, is created after the flow separation from walls and then diffuses with the fluid viscosity in three dimensions. It is a representative property to understand the formation, motion, and diffusion of vortices with the evolution of viscous fluids. Fig. 4 illustrates the instantaneous vorticity magnitudes ($\boldsymbol{\omega}\, d / U_0$) of the flow around a circular cylinder at Re = 3900. The shear layers extend from the sides of the circular cylinder, and the massive separation vortices account

for the modelled turbulence. Therefore, only the substantial vortex shedding is predicted using the URANS *k-ω* model, implying partial representative flow properties over cylindrical structures.

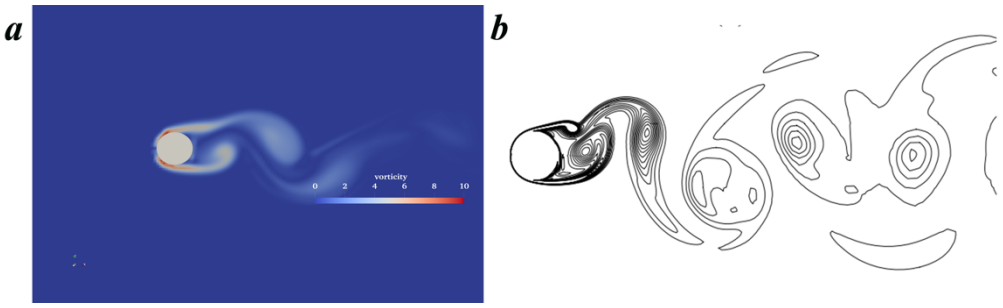

Fig. 4: The instantaneous vorticity magnitudes of flow over a circular cylinder at $Re = 3900$ (*a*: REEF3D URANS simulated results; *b*: URANS results in [40])

Additionally, the hydrodynamics around a 2D cylinder with a wider range of *Re* is studied and the results are presented in Fig. 5. Within the range of *Re* from 300 to 10^5, REEF3D predicts C_d with a good agreement compared to the empirical values and other simulation data. It is therefore concluded that 40 cells in the circumference of the cylinder is sufficient. Moreover, REEF3D overpredicts the drag forces slightly in the range of $10^3 < Re < 2.5 \times 10^3$, which is close to the transition area of laminar to turbulent flow. The deviation is still acceptable because the error is smaller than 8%.

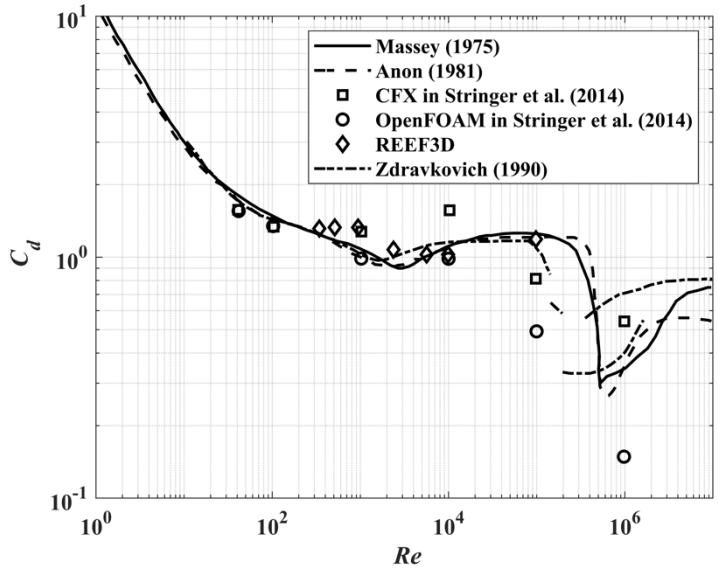

Fig. 5: Drag coefficient versus Reynolds number; correlation between experimental and numerical results. Published data for smooth cylinder: Zdravkovich (1990) [26], Massey (1975) [27], Anon (1981) [28], CFX / OpenFOAM [24].

To test the performance of the flow around a 3D structure, a cruciform case (Fig. 6a), which has been investigated in [19] numerically and in [12] experimentally, is used to validate the accuracy of REEF3D. The results are shown in Fig. 6b. The deviation between the results in [19] and REEF3D are small, which emphasizes that the chosen cell configuration is acceptable for further studies.

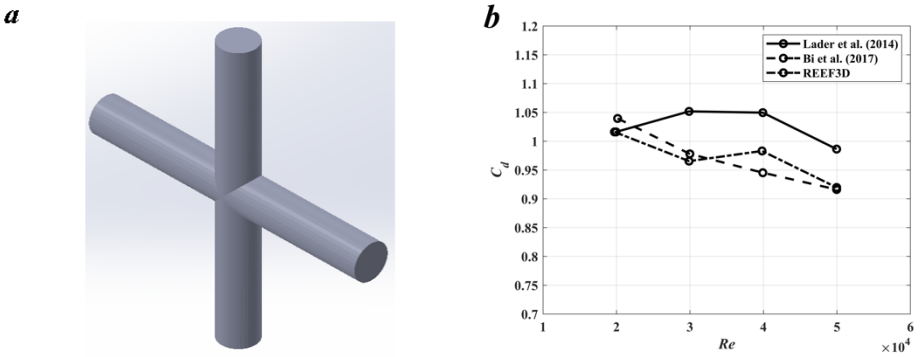

Fig. 6: ***a.*** Geometry in cruciform. ***b.*** Drag coefficient vs. Reynolds number for REEF3D and the laboratory experiment on a cruciform element [12].

3 Results and discussion

3.1 Flow around net meshes of different number

Three cases with a different number of net meshes, which is 1×1 (Case 1), 2×2 (Case 2), and 3×3 (Case 3), are considered to study the flow patterns around meshes. The diameter and length of each twine remain the same as the prototype. Generally, knots and mesh centers of a net panel are the areas with significant flow oscillations due to the local acceleration of the fluid along with the twines [25]. Due to the symmetrical properties of net meshes, several probe lines at critical locations (Fig. 7) in the x-direction are adopted to measure the magnitudes of velocity fluctuations in the mesh centers. The region close to the outlet boundary is neglected to diminish the irrelevant effect of the outflow condition. It is evident that the velocity drops rapidly at each knot and increases gradually in the downstream area. It is attributed to the formation of a vortices after flowing through the structures, which leads to the decrease of the flow velocity. Behind the vortex, the downstream velocity increases again to the incoming velocity based on the conservation laws. The downstream velocity approaches the incoming velocity in P2 locations of three cases, while the velocity across the central knot in Case 2 is 10% smaller than the

incoming velocity suggesting a variations of velocity reductions across intersections. Furthermore, the P2 of Case 2 and Case 3 show a similar variation while that of Case 1 recovers slower after passing the net meshes. These observations are consistent with the distributions of the velocity behind knots in the one-cruciform and four-cruciform patterns (as Case 1) in [19][35]. But, the observed larger oscillations of the velocity in P2 for the Case 2 and Case 3, including more cruciform frames, indicates that cross-flow effects around surrounding net meshes lead to considerable local accelerations behind knots. Additionally, the cross-flow fluctuates around the central knot and the edge locations, as given for Case 2. It can be concluded that the flow field behind varies meshes is influenced by the local fluid interactions which account for the wake reductions. Therefore, the adoptions of 1×1 mesh (four-cruciform) or the isolated one-cruciform configuration is not sufficient to study the flow around net meshes.

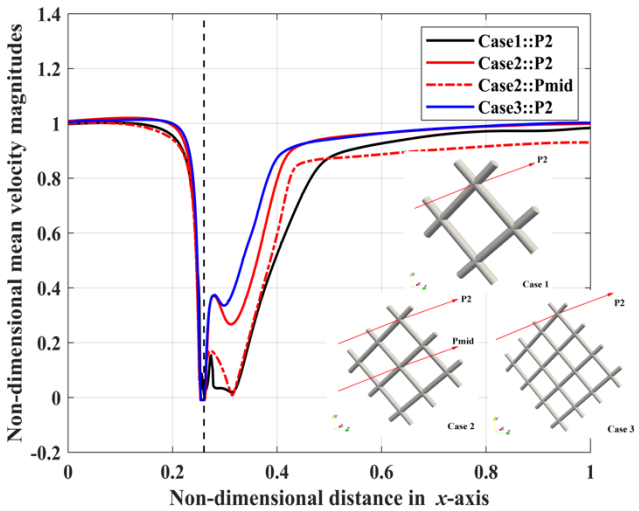

Fig. 7: Non-dimensional velocity magnitudes along the probe lines through the knot positions of three-sized meshes.

Next, Fig. 8 shows the velocity profile along the probe lines through the mesh center of each case. It is sufficient to consider the flow of only four-probe lines in the 9-mesh Case 3 due to symmetry. It is illustrated in Fig. 8 that the flow velocity increases sharply and then drops with different slopes at varied downstream distances which is in accordance with the findings in [19][35]. The flow in front of the structure is blocked to a small extent by the net. Afterward, a local acceleration of the flow at the mesh center appears due to the flow separation at the cylindrical-shaped net twines. The velocity reduction is significant as the downstream velocity decreases to around 85% of the incoming velocity. The velocity

increases slowly over the distance but is still lower than the incoming velocity except for Case 1. This is due to the increasing shielding effect of the net with more cruciform in a small portion of net panels. In comparison to the three-sized mesh, Case 2 and Case 3 show the identical velocity difference. In contrast, Case 1 shows the smallest distance of velocity reduction in the downstream region. Sn or so-called blockage ratio [36] is generally correlated to flow distributions of cylindrical cruciform, keeping the same among three-sized meshes. However, it can be concluded that the flow fields around the center of apertures and behind knots in four-cruciform (Case 1) or single set shows a significant diversity compared to the other cases covering more crossed cylinders, wherein S_n keeps the same invariably.

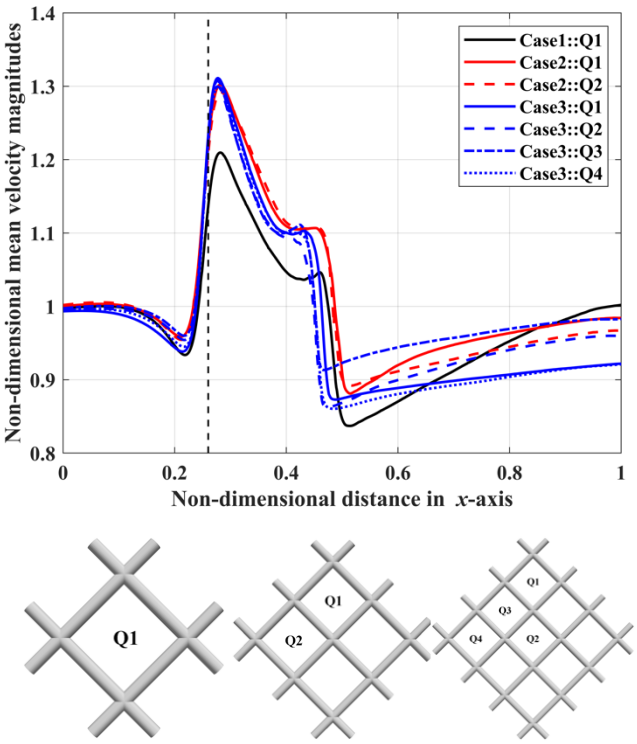

Fig. 8: Non-dimensional velocity magnitudes along the probe lines around mesh center of each case and the positions of each probe lines through incoming stream direction in three-sized net meshes.

The pressure distributions, as another important property of the flow field, define the induced hydrodynamic loadings on cylindrical structures. As the flow approaches the cylindrical bars, a high-pressure area is formed while the flow velocity reduces due to Bernoulli's principle. After the flow separates from the surface, a local negative pressure region is created behind the cylinder, resulting in a positive hydrodynamic drag force. In this part, two sampling planes are extracted and shown in Fig. 9. They cover the critical area for hydrodynamic fluctuations. The time-averaged pressure contours in Plane

1 and Plane 2 of the three-sized mesh cases are illustrated in Fig. 10. The local negative-pressure area behind the knot is more distinct than the area behind the net twines due to the larger areas occupied by the knots. Another possible interpretation lies in the formation of secondary flow induced by the intersection of orthometric cylinders, leading to higher pressure in the separation zone close to the surface around the intersection center [37~38]. Furthermore, the interactions of fluid can be visualized through the same local range of pressure magnitudes amongst adjacent net bars or knots. It is interesting to note that the local positive pressure contours deviate from the geometric symmetry axis of bars or intersections, showing a symmetrical tendency with respect to the net panel centers. It is attributed to the induced net solidity and the limited aperture area in each mesh which resembles the flow profiles around bluff bodies. Besides, the observations in this paper contradicts the assumption in [39] that the hydrodynamic interactions between net meshes can be overlooked in case of $l / d > 5 \sim 6$.

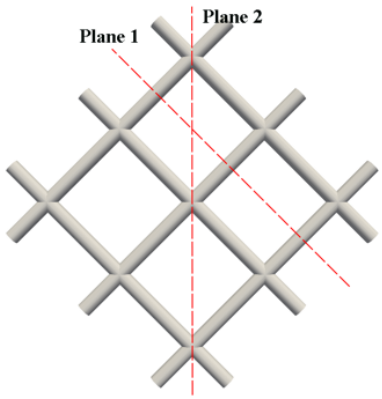

Fig. 9: Definition of the sampling planes slicing through the net panel.

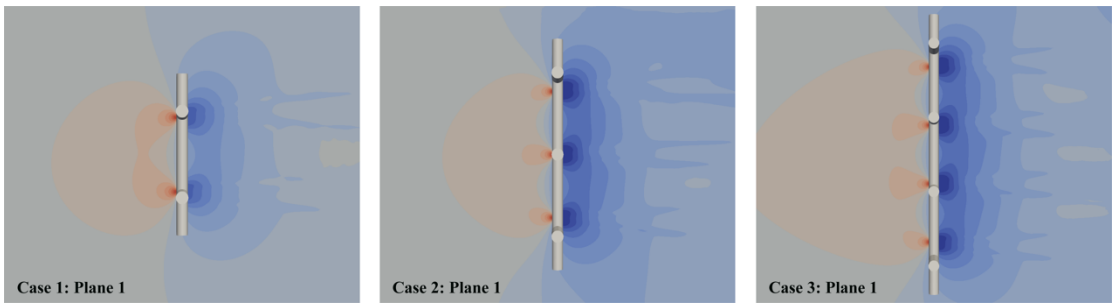

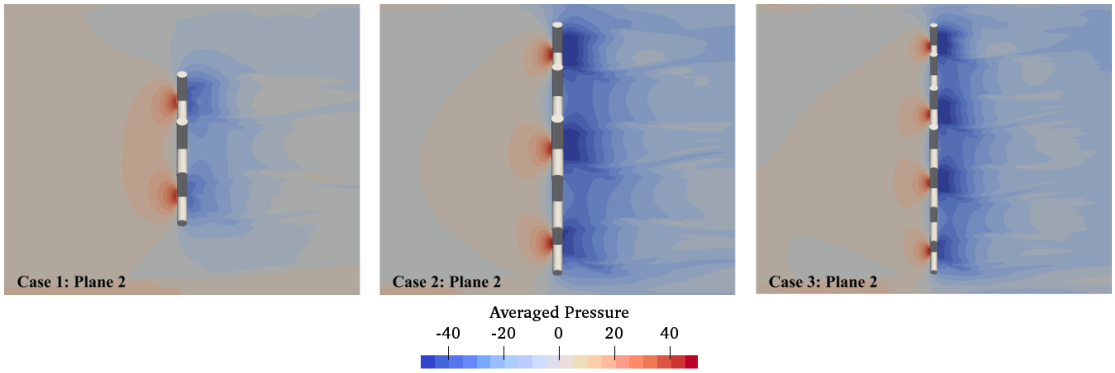

Fig. 10: The time-averaged pressure contours in Plane 1 and Plane 2 of three-sized meshes cases.

3.2 Hydrodynamics and flow around net meshes with different solidity ratio (S_n)

3.2.1 Hydrodynamic loadings

In the following, the 4-mesh pattern is chosen to study the effect of different net solidities on the hydrodynamic loadings and expected flow field. Generally, the first way to change S_n is to change the diameter of the net bars. Thus, Re is changed at the same time. In contrast, changing the length of twines to control S_n, does not change Re. In order to find a relationship for C_d based on Re and S_n, more cases with a wider range of Re (800 ~ 2200) are carried out based on the second method to control S_n (Case 9 ~ Case 31, shown in Table 2). The relationship between C_d, Re and net solidity is shown in Fig. 11. Here, it can be seen that C_d shows an increasing trend with increasing S_n. Especially for S_n = 0.2 ~ 0.28, the increasing rate is more than 20%. Further, C_d increases firstly and then decreases gradually with Re when S_n is larger than 0.2. The dependences of Re and S_n on C_d in this research remain consistent with the results in [13] and [14]. Additionally, it is obvious that S_n has a more significant influence on C_d than Re. Based on these observations, polynomial regression is used to fit the data of cases with varying lengths and S_n. The resulting semi-empirical formula (Eqn. 5 and Tab. 3) can be used to estimate C_d of nets with different S_n and Re. The fitting rate is 0.95, i.e., the goodness of fit is acceptable.

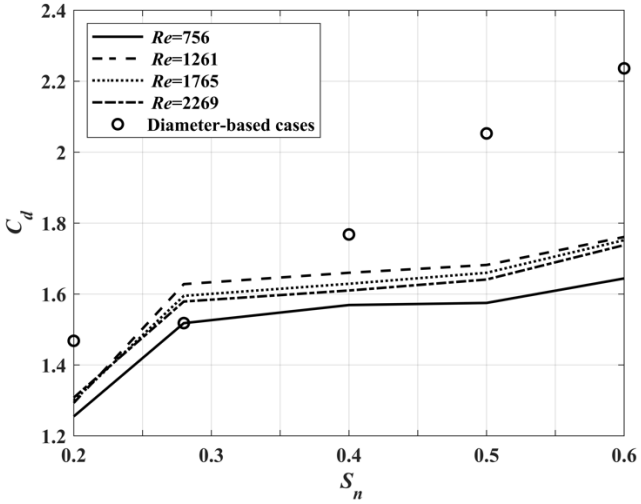

Fig. 11: Variations of C_d with Re and S_n (through length and diameter)

$$C_d = p00 + p10*Re + p01*S_n + p20*(Re\text{^}2) + p11*Re*S_n + p02*(S_n\text{^}2) + p21*(Re\text{^}2)*S_n + p12*Re*(S_n\text{^}2) + p03*(S_n\text{^}3) \quad (5)$$

Tab. 3: Values for the polynomial fitting of the drag coefficient (Eqn. 5).

Coefficients	Values
p00	-1.497
p10	0.0002193
p01	21.84
p20	-3.989e-08
p11	5.318e-05
p02	-52.25
p21	-1.697e-07
p12	0.0006487
p03	39.66

Moreover, the dependency of C_d on Re and S_n on basis of changing the diameter of the twines is depicted in Fig. 11 as well. For some cases, C_d is significant larger compared to cases for varying lengths, and the increasing rate of C_d against S_n is more critical. This indicates that Re effects also account for a change of the hydrodynamics. This is further validated through the flow field distributions given in the following section.

3.2.2 Flow field around meshes with different solidity ratio (S_n)

Two probe-lines in x direction, located in the regions of significant variations of flow, are selected to detect the magnitudes of the velocity oscillation (see Fig. 12). Firstly, we set up S_n ranging from 0.2 to 0.6 by changing the diameters of the net bars and keeping the length of all net bars consistent with the

prototype. From Fig. 12, Pmid-the middle node of mesh shows that the velocity decreases fast without significant difference at the upstream area in all cases with various S_n. Afterwards, it increases with different rates for varying S_n. The increasing rates for smaller S_n are 10% larger than that of cases with larger S_n, and the case with the smallest solidity ratio shows the largest downstream velocity. However, it is significant that larger S_n cases show a greater increase than smaller S_n cases around the mesh center. The flow in the largest S_n case is accelerated by more than 1.6 times the incoming velocity. It is explained by the larger radius of the cylinder resulting in an increased fluid separation and acceleration. After passing the meshes, the extent of velocity reduction of cases with larger S_n are more significant compared with that of smaller S_n cases. The interaction of the vortices at the downstream area for the large S_n cases yields a considerable velocity reduction which takes longer distance to achieve a steady state compared to small S_n cases (Fig. 13). In the far-field of the downstream region, the velocity reduction is more critical for the larger S_n cases. It is demonstrated in Fig. 13 that areas of negative pressure increase with the net solidities and can cover most parts of the wake behind the net panel. In contrast, the areas of increased positive pressure keep roughly the same amongst the three cases, and only the magnitudes increase with S_n. Moreover, the streamwise vorticity develops due to the separation of shear layers on both sides of the net twines as presented in Fig. 13. The extension of the shear layers become more noticeable with the increase of the solidity ratio. No obvious vortex shedding is observed behind the cylindrical meshes with increasing Re and S_n, which can be attributed to the suppression effect of intersections and spanwise cylinders [36] and application of an URANS CFD model. A high-fidelity turbulence model resolving the turbulence in the flow is necessary to study the fluid patterns in the wake within future research.

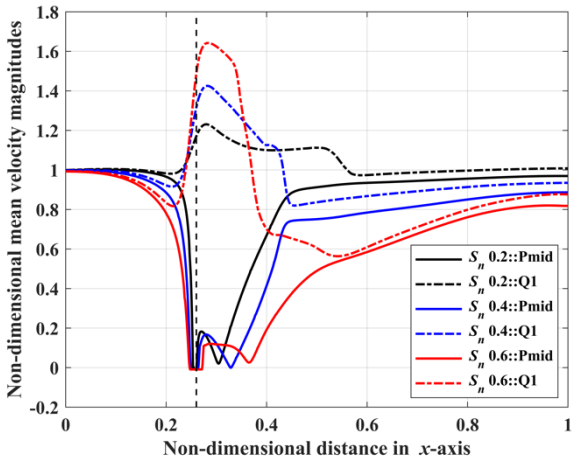

Fig. 12: Non-dimensional mean velocity magnitudes along the probe lines among cases with varied S_n (varied diameters).

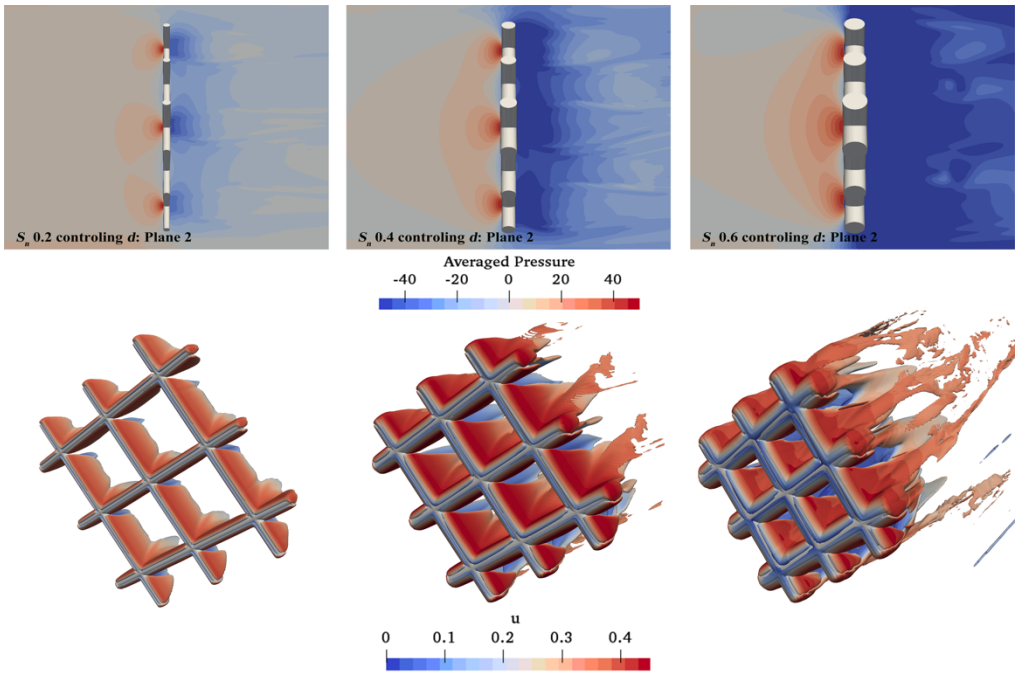

Fig. 13: The time-averaged pressure contours in Plane 2 and iso-surfaces of instantaneous streamwise vorticity ($\omega_z d / U_0 = \pm 1$) of three cases with S_n controlled by diameters.

Next, the length of the net twines is changed to vary S_n between 0.2 and 0.6, while the diameter is kept unchanged. As depicted in Fig. 14, the flow patterns are different from above, especially in the area after passing the mesh. “Pmid” shows that the velocity decreases fast without significant change in the upstream area for all cases. Then, it increases gradually close to the values of the incoming velocity,

which is dependent on net solidities as above. Moreover, the velocities at the mesh center increase sharply at first in all cases and then decrease to the incoming velocity value. The maximum velocity due to the local accelerations around the mesh in all S_n cases are the same, which is about 1.2 ~ 1.3 times the incoming velocity. After the flow passes the mesh, the velocity reduction is more significant for larger S_n cases compared to smaller S_n cases. In the far-field, the velocity stabilizes to the value of the incoming velocity for the case with S_n = 0.2, while 10% ~ 20% velocity reductions can be seen for the larger S_n cases in steady state. Similarly, the pressure around the net panels has the trend of increasing with S_n (Fig. 15) but the influencing area of both, positive and negative pressure zones, change little in this part.

The difference of the hydrodynamic loadings on net meshes with increasing S_n obtained from different geometrical net configurations can now be seen by comparing Fig. 15 to Fig. 13. The drop of the pressure between the cases with varying lengths is less significant than that within cases of varying diameters. Therefore, the hydrodynamic loads on the former nets are smaller than on the latter. From the iso-surfaces of the instantaneous streamwise vorticity, the development of large and unbroken shear layers separating from the cylinder surfaces can be noticed. They increase with solidity due to the constant *Re* during this variation.

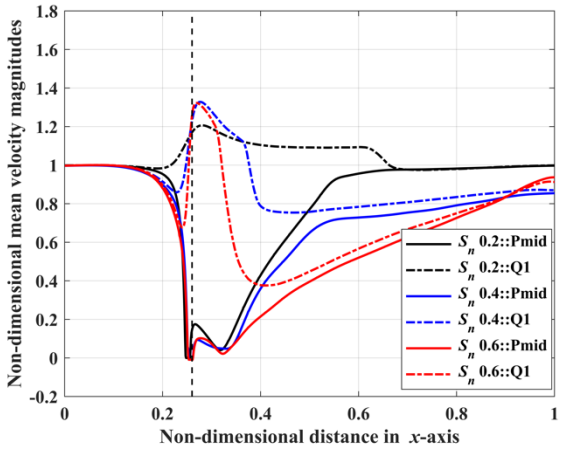

Fig. 14: Non-dimensional mean velocity magnitudes along the probe lines among cases with varied S_n (varied lengths)

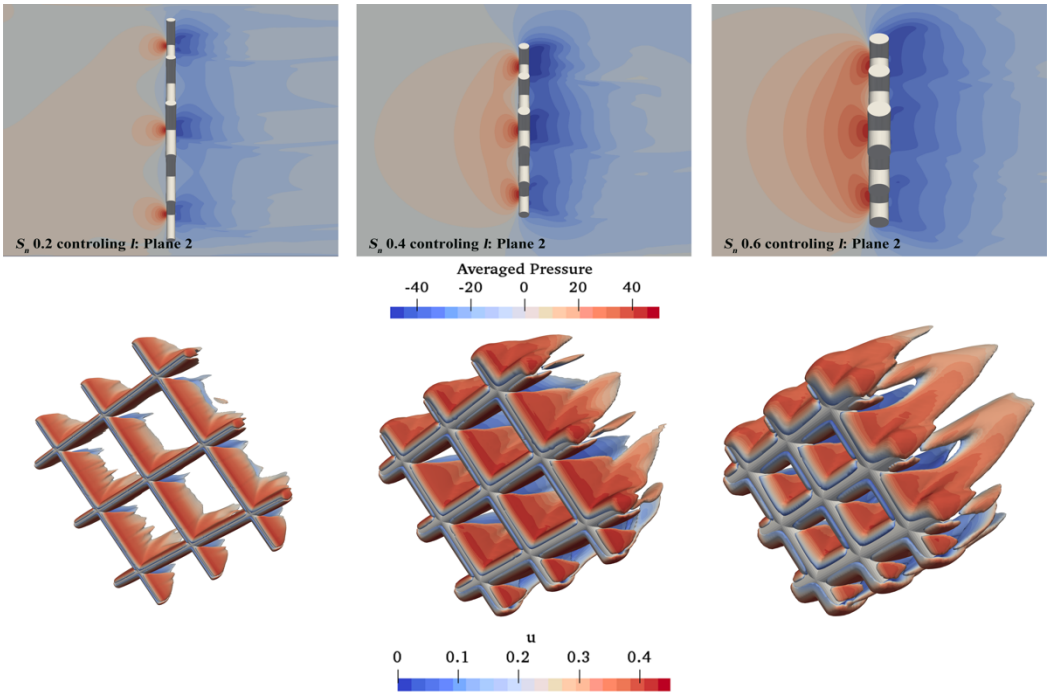

Fig. 15: The time-averaged pressure contours in Plane 2 and iso-surfaces of instantaneous streamwise vorticity ($\omega_z d / U_0 = \pm 1$) of three cases with S_n controlled by lengths

4 Conclusion

In this paper, the fluid properties around and the hydrodynamic loadings on net meshes are studied using the CFD model REEF3D. The accuracy of the numerical model is validated for the flow around a circular cylinder and a 3D cruciform using mean velocity and instantaneous vorticity profiles as well as drag coefficients. Then, the flow around 1 × 1, 2 × 2, and 3 × 3 mesh configurations is analysed to discuss the appropriate number of meshes in a numerical study. It is concluded that the flow field around the center a 1 × 1 mesh shows significant different patterns than for other cases covering more crossed cylinders and intersections. 2 × 2 and 3 × 3 mesh cases are more reliable when studying the flow around net meshes and wake patterns because the flow interactions around the net bars and the effects from the surrounding meshes are considered. Furthermore, the effect of the net solidity, including two strategies controlling this ratio, on the hydrodynamic drag and the flow field is studied. The simulations indicate that the net solidity has a more significant influence on the expected hydrodynamic drag than the Reynolds number, which is identical to the findings in [13] and [14]. A semi-empirical formula for the drag coefficient as a dependency on the solidity ratio and Reynolds number is subsequently derived. It is further presented that the two ways of controlling the solidity ratio have different effects on the fluid

patterns around and the hydrodynamic loadings on net meshes. The larger solidity ratio cases altered by diameters are predicting larger hydrodynamic drags compared to the larger solidity ratio cases obtained from decreasing the lengths of the bars. This is also confirmed through a larger negative pressure region for the former cases. The reason for the difference of the hydrodynamics is the effect of the changing Reynolds number introduced by the variation of the diameters of the bars. Besides, the development of shear layers separating from the cylinder surface becomes significant with the increase of the solidity. Here, the observations of the instantaneous streamwise vorticity validated the statement in [36] that the existence of intersections and spanwise cylinders suppress excessive vortex shedding. Through the comparisons between vorticities profiles, it can be concluded that with increasing Reynolds number the massive shear layers start breaking and scattering.

Within future studies, the turbulence in form of the fluctuations of turbulence intensity and dissipation rates should be discussed. Besides the significant velocity reductions and fluctuations in the wake of fish cages, the effect of turbulence on the circulations of micro-organisms in the cages should be considered carefully [41]. The production and dissipation of turbulent kinetic energy while passing the nets should be thereby studied in detail. The required improvement of the turbulence prediction implies the adoption of LES. Additionally, more factors concerning the hydrodynamics and flow around the net meshes can be considered such as the roughness of the material and the angle of attack between fluid and structure.

Acknowledgement

The study presented in the manuscript is supported by the National Key Research and Development Program of China (Project No. 2019YFD0901000), Research Council of Norway under the HAVBRUK2 project (No. 267981). The authors are grateful for the State Foundation for Visiting Ph.D. student from China Scholarship Council (No. 201906330049). This research was supported in part with computational resources at NTNU provided by The Norwegian Metacenter for Computational Sciences (NOTUR, http://www.notur.no) under project No. NN2620K.

References

[1] O.M., F., 2014, “Hydrodynamics of Marine and Offshore Structures,” *J. Hydrodyn.*, **26**(6), pp. 835–847.

[2] Zheng, Z. Q., Wan, R., Chang, Z. Y., Zhang, Y., and Tao, J., 2019, "Analysis of Plane Netting with Twine Breakage in Aquaculture Net Cage," *J. Mar. Sci. Technol.*, **27**(1), pp. 72–76.

[3] Li, L., Jiang, Z., Wang, J., and Ong, M. C., 2019, "Numerical Study on the Heading Misalignment and Current Velocity Reduction of a Vessel-Shaped Offshore Fish Farm," *J. Offshore Mech. Arct. Eng.*, **141**(5), pp. 051602.

[4] Choo Y, and Casarella MJ, 1971, "Hydrodynamic Resistance of Towed Cables," *J Hydronautics*, **5**(4), pp. 126–131.

[5] Miline P H, 1972, "Fish and Shellfish Farming in Coastal Waters," *Fishing News*, London, UK.

[6] Løland, G., 1993, "Current Forces on, and Water Flow through and around, Floating Fish Farms," *Aquac. Int.*, **1**(1), pp. 72–89.

[7] Zhan, J. M., Jia, X. P., Li, Y. S., Sun, M. G., Guo, G. X., and Hu, Y. Z., 2006, "Analytical and Experimental Investigation of Drag on Nets of Fish Cages," *Aquac. Eng.*, **35**(1), pp. 91–101.

[8] Zienkiewicz, O. C., 1980, "Viscous Flow."

[9] Balash, C., Colbourne, B., Bose, N., and Raman-Nair, W., 2009, "Aquaculture Net Drag Force and Added Mass," *Aquac. Eng.*, **41**(1), pp. 14–21.

[10] Hosseini, S. A., Lee, C. W., Kim, H. S., Lee, J., and Lee, G. H., 2011, "The Sinking Performance of the Tuna Purse Seine Gear with Large-Meshed Panels Using Numerical Method," *Fish. Sci.*, **77**(4), pp. 503–520.

[11] Kristiansen, T., and Faltinsen, O. M., 2012, "Modelling of Current Loads on Aquaculture Net Cages," *J. Fluids Struct.*, **34**, pp. 218–235.

[12] Lader, P., Enerhaug, B., Fredheim, A., Klebert, P., and Pettersen, B., 2014, "Forces on a Cruciform/Sphere Structure in Uniform Current," *Ocean Eng.*, **82**, pp. 180–190.

[13] Zhou, C., Xu, L., Hu, F., and Qu, X., 2015, "Hydrodynamic Characteristics of Knotless Nylon Netting Normal to Free Stream and Effect of Inclination," *Ocean Eng.*, **110**, pp. 89–97.

[14] Tang, H., Hu, F., Xu, L., Dong, S., Zhou, C., and Wang, X., 2017, "The Effect of Netting Solidity Ratio and Inclined Angle on the Hydrodynamic Characteristics of Knotless Polyethylene Netting," *J. Ocean Univ. China*, **16**(5), pp. 814–822.

[15] Patursson, Ø., Swift, M. R., Tsukrov, I., Simonsen, K., Baldwin, K., Fredriksson, D. W., and Celikkol, B., 2010, "Development of a Porous Media Model with Application to Flow through and around a Net Panel," *Ocean Eng.*, **37**, pp. 314–324.

[16] Zhao, Y. P., Bi, C. W., Dong, G. H., Gui, F. K., Cui, Y., Guan, C. T., and Xu, T. J., 2013, "Numerical Simulation of the Flow around Fishing Plane Nets Using the Porous Media Model," *Ocean Eng.*, **62**, pp. 25–37.

[17] Bi, C. W., Zhao, Y. P., Dong, G. H., Xu, T. J., and Gui, F. K., 2014, "Numerical Simulation of the Interaction between Flow and Flexible Nets," *J. Fluids Struct.,* **45**, pp. 180-201.

[18] Chen, H., and Christensen, E. D., 2017, "Development of a Numerical Model for Fluid-Structure Interaction Analysis of Flow through and around an Aquaculture Net Cage," *Ocean Eng.*, **142**, pp. 597–615.

[19] Bi, C. W., Balash, C., Matsubara, S., Zhao, Y. P., and Dong, G. H., 2017, "Effects of Cylindrical Cruciform Patterns on Fluid Flow and Drag as Determined by CFD Models," *Ocean Eng.*, **135**(March 2016), pp. 28–38.

[20] Bihs, H., Kamath, A., Alagan Chella, M., Aggarwal, A., and Arntsen, Ø. A., 2016, "A New Level Set Numerical Wave Tank with Improved Density Interpolation for Complex Wave Hydrodynamics," *Comput. Fluids*, **140**, pp. 191–208.

[21] Kamath, A., Chella, M. A., Bihs, H., and Arntsen, O. A., 2015, "Evaluating Wave Forces on Groups of Three and Nine Cylinders Using a 3D Numerical Wave Tank," *Eng. Appl. Comput. Fluid Mech.*, **9**(1), pp. 343–354.

[22] Martin, T., Kamath, A., and Bihs, H., 2020, "Modeling and Simulation of Moored-Floating Structures Using the Tension Element Method," *J. Offshore Mech. Arct. Eng.*, **142**(1), pp. 011803.

[23] Wilcox, D. C., 1993, Turbulence Modeling for CFD.

[24] Stringer, R. M., Zang, J., and Hillis, A. J., 2014, "Unsteady RANS Computations of Flow around a Circular Cylinder for a Wide Range of Reynolds Numbers," *Ocean Eng.*, **87**, pp. 1–9.

[25] Faltinsen, O. M., 2017, "Sloshing," *Adv. Mech.*, **47**(1), pp. 1–24.

[26] Zdravkovich, M. M., 1990, "Conceptual Overview of Laminar and Turbulent Flows Past Smooth and Rough Circular Cylinders," *J. Wind Eng. Ind. Aerodyn.*, **33**(1–2), pp. 53–62.

[27] Massey, B. S., 1975, "Mechanics of fluids," ((3rd edition, 1975)).

[28] Anon, 1981, "Mean Forces, Pressures and Flow Field Velocities for Circular Cylindrical Structures: Single Cylinder with Two-dimensional Flow.," *Eng. Sci. Data Unit*, Data Items.

[29] Aggarwal, A., Bihs, H., Myrhaug, D., and Chella, M. A., 2019, "Characteristics of Breaking Irregular Wave Forces on a Monopile," *Appl. Ocean Res.*, **90**, pp. 101846.

[30] Alagan Chella, M., Bihs, H., and Myrhaug, D., 2019, "Wave Impact Pressure and Kinematics Due to Breaking Wave Impingement on a Monopile," *J. Fluids Struct.*, **86**, pp. 94–123.

[31] Aggarwal, A., Bihs, H., Shirinov, S., and Myrhaug, D., 2019, "Estimation of Breaking Wave Properties and Their Interaction with a Jacket Structure," *J. Fluids Struct.*, **91**, pp. 102722.

[32] Martin, T., Kamath, A., and Bihs, H., 2019. Numerical Modelling of the Interaction between a Fish Net and Fluid using CFD. *Proceedings of VII International Conference on Computational Methods in Marine Engineering, MARINE 2019, Gothenburg, Sweden.*

[33] Martin, T., Kamath, A., and Bihs, H., 2019. Numerical Modelling of Net Motion in Waves and Current Using CFD. *Proceedings of 38th International Conference on Ocean, Offshore and Arctic Engineering, OMAE 2019.Volume 6. Glasgow, UK.*

[34] Fredheim, A., 2005. Current Force on Net Panels. *PhD Thesis*, Norwegian University of Science and Technology, Trondheim.

[35] Zou, B., Thierry, N. N. B., Tang, H., Xu, L., Zhou, C., Wang, X., Dong, S., and Hu, F., 2021, "Flow Field and Drag Characteristics of Netting of Cruciform Structures with Various Sizes of Knot Structure Using CFD Models," *Appl. Ocean Res.*, **106**, p. 102466.

[36] Tang, M. F., Dong, G. H., Xu, T. J., Bi, C. Wei, and Wang, S., 2020, "Large-Eddy Simulations of Flow Past Cruciform Circular Cylinders in Subcritical Reynolds Numbers," *Ocean Eng.*, p. 108484.

[37] OSAKA, H., NAKAMURA, I., YAMADA, H., KUWATA, Y., and KAGEYAMA, Y., 1983, "The Structure of a Turbulent Wake behind a Cruciform Circular Cylinder: 1st Report, The Mean Velocity Field," *Bull. JSME*, **26**(213), pp. 356–363.

[38] OSAKA, H., YAMADA, H., NAKAMURA, I., KUWATA, Y., and KAGEYAMA, Y., 1983, "The Structure of a Turbulent Wake Behind a Cruciform Circular Cylinder : 2nd Report, The Streamwise Development of Turbulent Flow Field," *Bull. JSME*, **26**(214), pp. 521–528.

[39] Løland, G., 1991, "Current Forces on and Flow through Fish Farms," *PhD Thesis*, NTNU, Trondheim, Norway.

[40] Young, M. E., and Ooi, A., 2007, "Comparative Assessment of LES and URANS for Flow over a Cylinder at a Reynolds Number of 3900," *Proceedings of the 16th Australasian Fluid Mechanics Conference*, 16AFMC, pp. 1063–1070.

[41] Klebert, P., and Su, B., 2020, “Turbulence and Flow Field Alterations inside a Fish Sea Cage and Its Wake,” *Appl. Ocean Res.*, **98**, p. 102113.